Detection of supercooled liquid in mixed-phase clouds using radar Doppler spectra

Edward P. Luke,[1] Pavlos Kollias,[2] and Matthew D. Shupe[3]

Received 27 July 2009; revised 2 February 2010; accepted 30 March 2010; published 1 October 2010.

[1] Cloud phase identification from active remote sensors in the temperature range from 0 to −40°C, where both liquid and ice hydrometeor phases are sustainable, is challenging. Millimeter wavelength cloud radars (MMCR) are able to penetrate and detect multiple cloud layers. However, in mixed-phase conditions, ice crystals dominate the radar signal, rendering the detection of liquid droplets from radar observables more difficult. The technique proposed here overcomes this fundamental limitation by using morphological features in MMCR Doppler spectra to detect supercooled liquid droplets in the radar sampling volume in the presence of ice particles. High lidar backscatter and near-zero lidar depolarization measurements (good indicators of the presence of liquid droplets) from the Mixed-Phase Arctic Clouds Experiment (MPACE) conducted in Barrow, Alaska, are used to train the technique and evaluate its potential for detecting mixed-phase conditions. Ceilometer, microwave radiometer, and radiosonde measurements provide additional independent validation. Because of the ability of MMCRs to penetrate multiple liquid layers, this radar-based technique does not suffer from the extinction limitations of lidars and is thus able to expand cloud phase identification methods to cloud regions beyond where lidars can penetrate, providing output at the native radar resolution. The technique is applicable to all profiling radars that have sufficient sensitivity to observe the small amount of liquid in mixed-phase clouds.

Citation: Luke, E. P., P. Kollias, and M. D. Shupe (2010), Detection of supercooled liquid in mixed-phase clouds using radar Doppler spectra, *J. Geophys. Res.*, *115*, D19201, doi:10.1029/2009JD012884.

1. Introduction

[2] The life cycles and radiative properties of clouds are highly sensitive to the phase of their hydrometeors (i.e., liquid or ice). Current cloud parameterizations that partition water into liquid and ice based on temperature are characterized by large uncertainties [*Curry*, 1986; *Hobbs and Rangno*, 1985; *Intrieri et al.*, 2002]. These uncertainties are particularly important in high geographical latitudes and temperature ranges where both liquid droplets and ice crystals can coexist (mixed-phase cloud). Furthermore, the presence of both ice and liquid affects the macroscopic properties of clouds including their propensity to precipitate.

[3] Mixed-phase clouds have a major presence in global cloud cover [*Hogan et al.*, 2004]. Cloud phase classifications made at the Atmospheric Radiation Measurement (ARM) North Slope of Alaska (NSA) observation site over the past 6 years and similar results from the yearlong Surface Heat Budget of the Arctic (SHEBA) project have shown that mixed-phase clouds occur approximately 45% of the time in the Arctic [*Shupe et al.*, 2006] with maximum occurrence during the spring and fall transition seasons. These Arctic mixed-phase clouds are typically stratiform in nature, occur at the top of the inversion-capped boundary layer, often contain little liquid water, and are remarkably persistent (sometimes lasting for days to weeks). The liquid water found in these mixed-phase clouds, even in the cold polar winter, has been shown to play the dominant role in cloud-surface radiative interactions [*Shupe and Intrieri*, 2004] and can have profound impacts on the start and duration of the melt season, on the total extent and thickness of sea ice, and indirectly on the annual evolution of the surface albedo [e.g., *Zhang et al.*, 1996; *Maykut and Untersteiner*, 1971]. In the midlatitudes, in addition to radiative implications, mixed-phase clouds also have great importance with respect to aircraft icing hazards [*Cober et al.*, 2001].

[4] Mixed-phase clouds are understudied compared to arguably simpler single-phase clouds because of a number of observational limitations. In situ measurements in mixed-phase clouds are hindered because of aircraft icing hazards, difficulties distinguishing hydrometeor phase, and discrepancies in methods for deriving physical quantities [*Wendisch et al.*, 1996; *Lawson et al.*, 2001]. At high latitudes, satellite-based retrievals of cloud phase are often hindered by the highly reflective ice-covered ground and persistent temperature inversions. In spite of these hindrances, observational studies of mixed-phase clouds have been possible in some

[1]Atmospheric Sciences Division, Brookhaven National Laboratory, Upton, New York, USA.
[2]Department of Atmospheric and Oceanic Sciences, McGill University, Montreal, Quebec, Canada.
[3]Cooperative Institute for Research in Environmental Sciences, University of Colorado and NOAA, Boulder, Colorado, USA.

0148-0227/10/2009JD012884

conditions using aircraft observation campaigns [*Hobbs and Rangno*, 1998; *Pinto*, 1998; *Lawson et al.*, 2001; *Korolev et al.*, 2003], routine satellite observations [*Wang and Key*, 2003], and multisensor observations from operational ground stations [*Hogan et al.*, 2003; *Wang et al.*, 2004; *Turner*, 2005; *Shupe et al.*, 2006]. A comprehensive overview of remote sensing–based retrieval techniques in mixed-phase clouds is provided in the work of *Shupe et al.* [2008].

[5] In this study, we use measurements from the U.S. Department of Energy (DOE) Atmospheric Radiation Measurement (ARM) program Mixed-Phase Arctic Clouds Experiment (MPACE) [*Verlinde et al.*, 2007] conducted in the fall of 2004 at the North Slope of Alaska (NSA) site [e.g., *Stamnes et al.*, 1999; *Ackerman and Stokes*, 2003]. During the experiment, collocated measurements from the University of Wisconsin High Spectral Resolution Lidar (HSRL) [*Eloranta*, 2005] and the ARM program millimeter wavelength cloud radar (MMCR) [*Moran et al.*, 1998] were collected. Prior to MPACE, the NSA MMCR receiver was upgraded [*Kollias et al.*, 2007] and continuous recording of the MMCR Doppler spectra was available. The MMCR Doppler spectrum reports the full distribution of the return echo over a range of Doppler velocities, through which it is capable of providing detailed information about cloud microphysics and dynamics [e.g., *Kollias et al.*, 2002]. Before the upgrade, only the first three moments of the Doppler spectrum were recorded, namely the zeroth moment or radar reflectivity, the first moment or mean Doppler velocity, and the second moment or Doppler spectrum width. These three moments of the Doppler spectrum are sufficient to describe the spectrum shape if it does not deviate significantly from the Gaussian distribution (moment approach). In mixed-phase conditions, the moments are dominated by the ice crystals' characteristics and the detection of supercooled liquid is very difficult, although spectrum width can provide useful information [*Shupe*, 2007].

[6] Our objective is to demonstrate that we can overcome the inability of the radar moment approach to detect the presence of supercooled liquid in mixed-phase conditions through careful analysis of recorded Doppler spectra from the vertically pointing radars of the ARM program (spectral approach). Our technique looks beyond the traditional moment approach in the analysis of cloud radar observations and attempts to retrieve microphysical properties from the typically skewed, often multimodal, and sometimes very complex morphologies of cloud radar Doppler spectra [*Kollias et al.*, 2007a]. These distortions result from the interplay of cloud dynamics, microphysics, and cloud phase. We decompose the Doppler spectra into several bands of differing resolution, each localized in Doppler velocity, using continuous wavelet transforms and analyze the resulting patterns with a neural network.

[7] Since we do not have direct measurements of the spatial distribution of liquid in the atmospheric column, we use the next best available proxy, collocated measurements of lidar backscatter (β) and circular depolarization (CDR) to train and validate our retrieval algorithm. Additional validation (but not algorithm training) is provided by integrated liquid water path measurements from a collocated microwave radiometer. First, we demonstrate that the radar-based retrieval technique accurately predicts the presence of supercooled liquid in mixed-phase clouds using the radar Doppler spectra as the only input. Second, we demonstrate that the technique is capable of predicting with reasonable success the lidar signals (β and CDR) from the Doppler spectra.

2. Background

[8] From the ground, the retrieval of mixed-phase cloud properties has been the subject of extensive research over the past 20 years using polarization lidars [e.g., *Sassen et al.*, 1990], dual radar wavelengths [e.g., *Gosset and Sauvageot*, 1992; *Sekelsky and McIntosh*, 1996], combined active and passive sensors [*Wang et al.*, 2004; *Turner*, 2005; *Shupe*, 2007], and, recently, radar Doppler spectra [*Shupe et al.*, 2004, 2008]. Millimeter-wavelength radars have substantially improved our ability to observe nonprecipitating clouds [*Kollias et al.*, 2007b] because of their superior sensitivity to nonprecipitating cloud layers and their ability to penetrate several cloud layers.

[9] In clouds, lidar backscatter β ($sr^{-1}m^{-1}$) is proportional to the square of the diameter (D) of the hydrometeors ($\sim D^2$). Depolarization of lidar backscatter (circular depolarization ratio, CDR) indicates that the scattering particles are nonspherical (when multiple scattering is negligible). In typical mixed-phase conditions, liquid occurs as a high concentration of small spherical droplets while ice is distributed in relatively lower concentrations of large, nonspherical ice crystals. As a result, the lidar backscatter ($\sim D^2$) signal is dominated by the high-concentration liquid droplets; areas with high-intensity lidar backscatter and near-zero lidar depolarization signals indicate the presence of small liquid droplets. On the contrary, the radar backscatter is proportional to the sixth power of the hydrometeor diameter ($\sigma \sim D^6$). Thus, in typical mixed-phase conditions, the low-concentration large ice crystals dominate the radar backscatter signal, which therefore offers little information about the spatial distribution of liquid in the atmospheric column. This is true if only the Doppler moments are available (moments approach). In general, clouds composed of only small liquid droplets do not have a reflectivity higher than −17 dBZ [*Frisch et al.*, 1995]. Thus, in subzero temperatures, higher reflectivities suggest the presence of larger particles such as ice crystals. When the conditions of high radar reflectivity (dBZ > −17), high lidar backscatter ($\beta > 5{\cdot}10^{-5}$ $sr^{-1}m^{-1}$), and near-zero lidar circular depolarization signal (CDR < 0.1) are observed simultaneously, this implies the presence of mixed-phase conditions. Such synergistic cloud phase retrieval schemes that use collocated radar and lidar profiles have been used in the past [e.g., *Shupe*, 2007]. However, synergistic radar/lidar techniques are limited to the maximum height the lidar penetrates before complete signal attenuation.

[10] In mixed-phase conditions, at least two-mode particle size distributions (PSD) with different phase, terminal velocity, and backscattering characteristics are present in the radar sampling volume. The terminal velocity of cloud droplets is negligible compared to typical vertical motions encountered in clouds, so that where ice crystals are not present the observed mean Doppler velocity is a very good indication of the vertical air motion [e.g., *Kollias et al.*, 2001; *Shupe et al.*, 2004]. In contrast, ice particles have larger and broader fall velocity distributions and account for most of the radar backscattered energy. If sufficient separation between liquid and ice fall velocity distributions exists, the spectra may

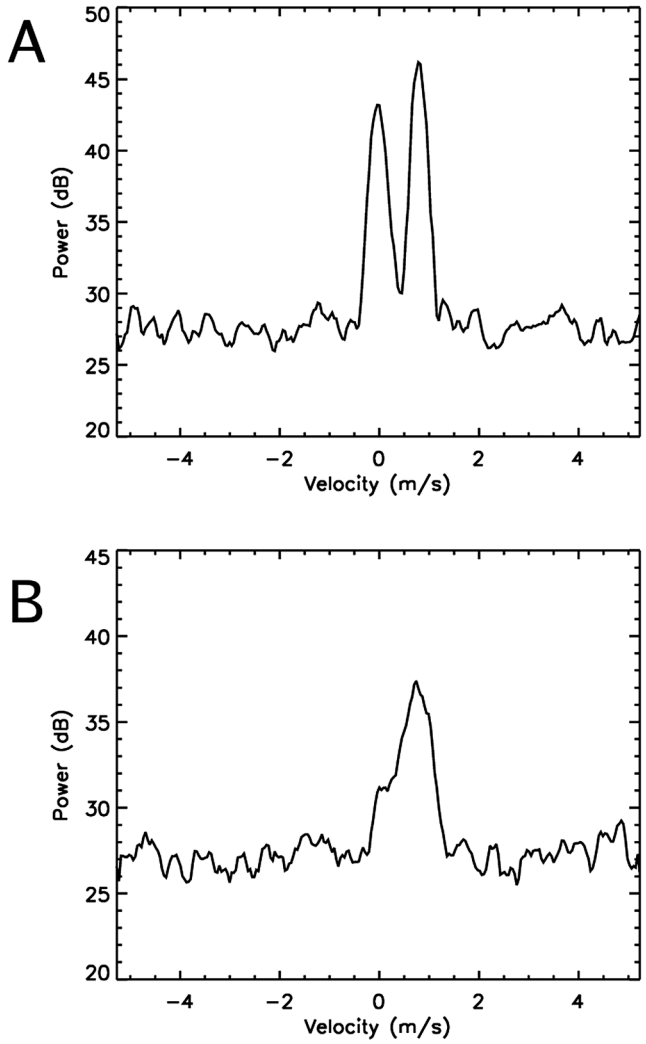

Figure 1. Examples of MMCR Doppler spectra generated from (a) two different phase mode particle size distributions with enough size separation to create a bimodal Doppler spectrum and (b) two different phase particle size distributions that do not have sufficient velocity difference to generate a clear bimodal Doppler spectrum separated by noise bins.

exhibit a pronounced bimodality (Figure 1a) that can be used to retrieve the vertical air motion and liquid and ice microphysics (e.g., liquid water content, ice water content, and ice effective radius) [*Shupe et al.*, 2004]. For the MMCR, negative Doppler velocity indicates motion away from the radar (upward). If there is not sufficient separation between liquid and ice fall velocity distributions, then often a skewed single-peaked Doppler spectrum is observed (Figure 1b). Such asymmetry features in the Doppler spectrum are not captured well using the traditional radar Doppler moments approach and can be a source of information about the presence of mixed-phase conditions.

[11] Cloud turbulence, however, can have an overwhelming effect and smear (smooth) such asymmetries induced by cloud microphysics. Recently, the ARM MMCRs deployed a new optimum sampling strategy, along with continuous recording of the Doppler spectra, which has been specifically designed to minimize the effects of turbulence on the spectra [*Kollias et al.*, 2007a] through a shortened dwell time and a smaller beam width and resolution volume. These new optimum MMCR sampling settings were operational at the NSA MMCR during the MPACE experiment. Our technique has been developed and tested largely under stratiform conditions. Performance would likely degrade in the turbulence of strong convection.

3. Extraction of MMCR Doppler Spectra Morphological Features

[12] Starting with the MMCR Doppler spectra, we remove the noise, eliminate artifacts (e.g., aliasing, spectral images) and identify the significant signal detections from hydrometeors [*Kollias et al.*, 2007a]. Then, we apply a second-order Gaussian continuous wavelet transform (CWT) to the spectra (Figures 2 and 3). The application of the CWT to a Doppler spectrum decomposes the spectral power into a two-dimensional array providing feature localization in both Doppler velocity and spectrum width (scale). This is accomplished by convolving the spectrum with a set of dilations a and translations b of a "mother wavelet" ψ, according to

$$\psi_{a,b}(v) = \psi\frac{v-b}{a}$$

where v is Doppler velocity [e.g., *Addison*, 2002; *Rioul and Vetterli*, 1991]. We refer to the parameter a as the scale of the wavelet. To demonstrate the ability of the CWT to detect and localize the components of a sum of Gaussians, we applied it to synthetically generated Doppler spectra (Figure 2). Figure 2a contains a Gaussian synthetic Doppler spectrum (i.e., unimodal particle size distribution). Figure 2b contains a synthetic Doppler spectrum generated from a pair of identical Gaussian distributions (i.e., bimodal particle distribution of equal radar reflectivity) resulting in a nonskewed spectrum. Figure 2c contains a Gaussian pair of unequal magnitude (i.e., liquid and ice particle size distributions), resulting in a skewed spectrum resembling many real spectra. The radar moment approach results in very similar Doppler moments for all three spectra, and thus, the subtle differences in the shapes of the three synthetic spectra may not be captured. The operation of the CWT at a scale appropriate to detect the fundamental Gaussian features on the synthetic spectra is shown in Figures 2d–2f. The coefficients are different in all three cases, indicating the ability to detect the subtle differences in the shapes of the synthetic Doppler spectra. The wavelet scale appropriate to detect the different particle modes is not known in advance. Thus, we apply the second-order Gaussian mother wavelet to each recorded MMCR Doppler spectrum at several different scales and use the output as input to a neural network to detect the presence of supercooled liquid in mixed-phase clouds.

[13] Figure 3 shows the complete set of parameters generated by the CWT for a typical mixed-phase Doppler spectrum. The observed Doppler spectrum (Figure 3b) presents evidence of skewness toward the low fall velocity edge of the spectrum due to the presence of liquid and ice particles in the radar sampling volume. The CWT is applied to the observed Doppler spectrum at six different scales (Figure 3a) and the resulting coefficients (Figure 3c) form most of the

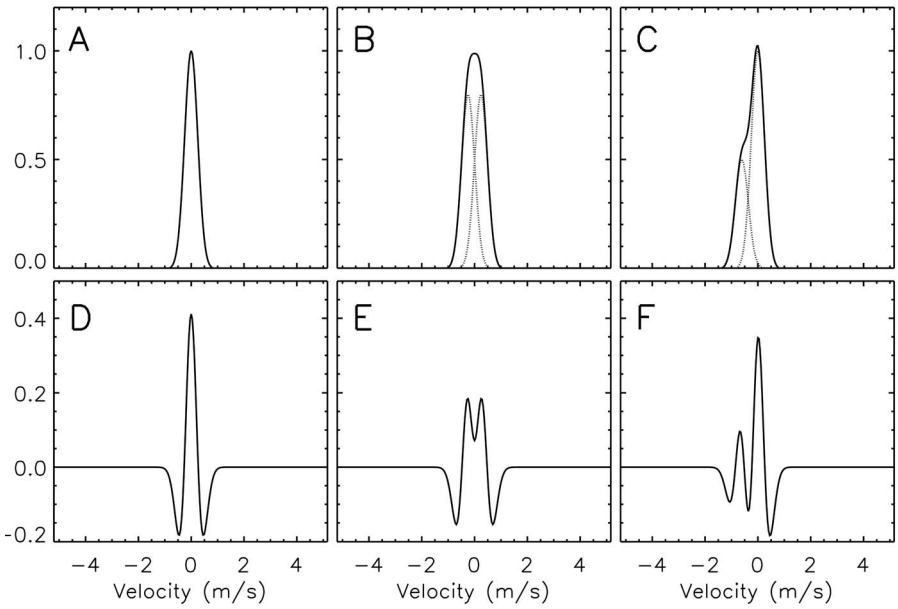

Figure 2. Synthetic MMCR Doppler spectra generated by (a) a single Gaussian distribution, (b) the superposition of two equal magnitude Gaussian distributions, (c) the superposition of two unequal magnitude Gaussian distributions, and (d–f) their corresponding continuous wavelet transforms.

input to the neural network. The radar reflectivity, mean Doppler velocity, and spectrum width of the Doppler spectrum significant peak, calculated independently of the CWT, complete the list of input parameters to the neural network. Parameters such as the radar range (altitude) and temperature are not inputs to the algorithm. The neural network learns the functional relationship between this full set of radar spectrum-based input parameters and the HSRL backscatter and depolarization measurements taken at the same time during MPACE.

[14] We now briefly describe the operation and training of the neural network. A neural network consists of a collection of interconnected processing elements, which in practice are organized in a manner tailored to the type of problem to be solved. Although sometimes implemented directly in specialized hardware, the processing elements are commonly, as in our application, a software abstraction running on a general purpose computer. Our retrieval technique uses the feedforward connection model, organizing processing elements into a structure known as a multilayer perceptron. Information flows in parallel through this structure along a clearly defined forward path from a set of continuous-valued inputs, through several stages of processing elements, to a set of continuous-valued outputs. Each processing element composing the network has itself a set of continuous-valued inputs $i_{1\ldots n}$, a single continuous-valued output o, a set of internal adjustable weights $w_{1\ldots n}$, and an internal adjustable bias b. The weights and bias are the sole means of controlling the behavior of processing elements and, in turn, the behavior of the entire neural network.

[15] Each processing element computes an internal activation when a pattern is applied to its inputs,

$$a = \mathbf{i} \cdot \mathbf{w} + b \ ,$$

and passes this value through a function, typically monotonically increasing and differentiable, to its output. In our case, this is the logistic sigmoid function,

$$o = f(a) = \frac{1}{1 + e^{-a}}.$$

Thus, the activation and output depend upon the amount of alignment between the input vector and the internal weights. When many such processing elements having different patterns of activation are interconnected, complex nonlinear behavior can be produced, with the overall computational task distributed across many processing elements.

[16] It is known that neural networks of this form can approximate arbitrary multidimensional continuous mappings [e.g., *Funahashi*, 1989]. In order to accomplish this, a neural network must have a sufficient number of processing elements and interconnections, and it must be trained on a particular mapping through a process such as the backpropagation of errors algorithm [*Rumelhart et al.*, 1986]. In our case, backpropagation establishes the ability to map radar Doppler spectrum features to HSRL backscatter and depolarization parameters. A representative set of paired input/output training data defines the mapping.

[17] During the training process, input vectors from the representative training data set (in our case, radar spectrum features) are applied sequentially to the neural network. As each is applied, the resulting output vector of the neural network is compared with the corresponding HSRL measurement from the representative training data set. The difference between the actual neural network output and the HSRL measurement (i.e., error) is then used to make a slight adjustment to the internal weights of all processing elements in a gradient descent process. As the training data are successively cycled through, the reduction in error is monitored, and when

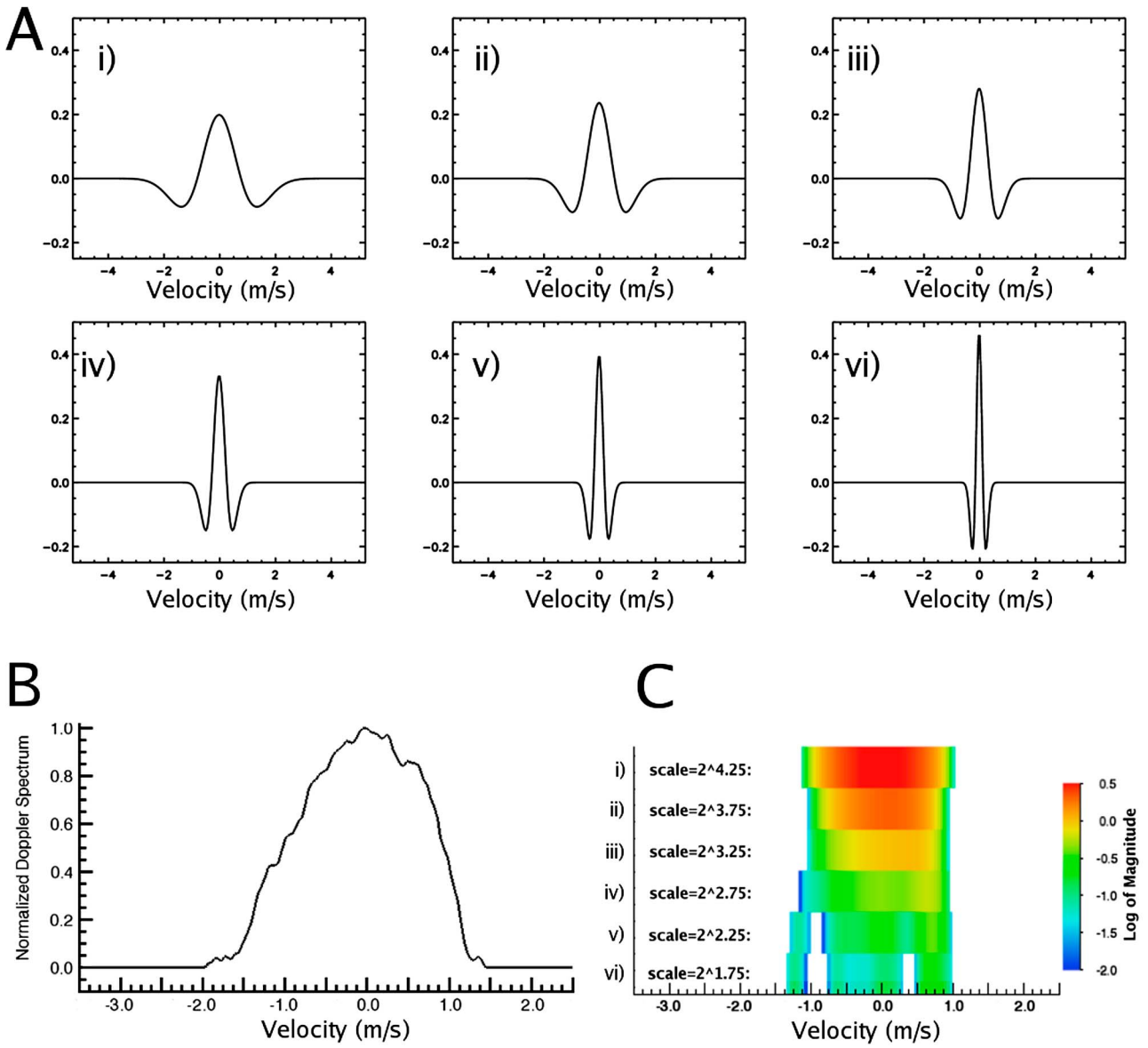

Figure 3. (a) The wavelet at each scale used, (b) example of an observed mixed-phase Doppler spectrum, and (c) the corresponding wavelet transform of the Doppler spectrum at each scale.

no more overall improvement is observed, the training process ceases. In practice, the monitoring of error reduction is usually performed on a second independent data set reserved for this purpose, known as the validation data. These data are never used to adjust weights and thus test the ability of the neural network to generalize beyond the training set. If training has been successful, the neural network, when presented with a novel input vector not previously encountered, will correctly map it to a corresponding output vector. In other words, it makes predictions of HSRL backscatter and depolarization values for new Doppler radar spectra not belonging to the representative training set.

[18] Figure 4 shows a scatterplot of the actual measured lidar CDR versus the measured lidar backscatter for most of the MPACE field study. We used a small fraction of these HSRL measurements to train the neural network. The boxed area in Figure 4 encloses lidar detections of supercooled liquid (clear separation from solid particle detections). To generate a radar-based supercooled liquid binary mask from new Doppler spectra, the trained neural network outputs predicted values of lidar CDR and backscatter associated with each spectrum, and a determination is made whether these predicted values fall within this same boxed area. Those that do constitute a liquid detection in the mask.

[19] The training data set was selected from the first 7 days of October 2004. The MMCR measurements have a vertical resolution of 45 m and temporal resolution of 5 s. Every 7 h of observations, 1 h of MMCR measurements and their corresponding nearest lidar measurements in time and height are selected (Figure 5). We decided to select training data every seventh hour (the choice of seven is arbitrary) so that the majority of time is not sampled, allowing abundant

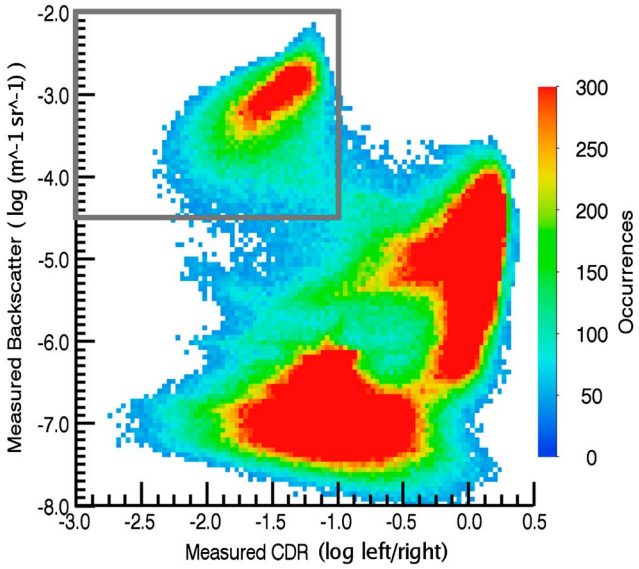

Figure 4. Measured lidar backscatter cross section versus circular depolarization ratio for most of October 2004 with the region corresponding to liquid detection outlined by a gray box.

intervals for testing the predictor's ability to generalize. The selected measurements are divided into two equal-sized groups. One group serves exclusively as the training data source, and the other is for validation. During each training cycle, the neural network output is evaluated over the validation data set. Iterations of the network for which an overall improvement occurs are saved. When there is no further improvement after 20,000 cycles, the process terminates.

4. Results

[20] To validate the performance of our classifier, we first show in detail several retrieved time-height liquid water masks that have good agreement with the independently measured ceilometer cloud base. Next, we show that good agreement between the base of the retrieved liquid mask and the ceilometer cloud base holds for the full month of October 2004. Finally, we demonstrate excellent long-term correlation between time series of our retrieved liquid mask's column thickness and the integrated liquid water path measured independently by a collocated microwave radiometer. We contrast this with a poor correlation between the total column thickness of significant radar detections and the same time series of Microwave Radiometer (MWR) liquid water path. In addition, we demonstrate from soundings that the measured thermodynamic conditions coinciding in time-height with our liquid mask are consistent with mixed-phase conditions.

4.1. Time-Height Liquid Mask Comparisons

[21] The neural network output (prediction of supercooled liquid location via prediction of lidar backscatter and lidar circular depolarization ratio) derived using MMCR Doppler spectra is evaluated with data collected during the ARM MPACE campaign. The first examined case is a deep cloud layer observed on 7 October 2004. Figure 6 shows the time-height mapping of the MMCR Doppler moments for a 1 h period (1000–1100 UTC). This hour is not included in the training data set. The observed MMCR reflectivities range from -15 to + 15 dBZ with distinct streaks of high radar reflectivity originating around 2 km altitude accompanied by increased Doppler velocities. In contrast, the highest Doppler spectrum width values are observed in the layer between 2 and 2.5 km. Temperature measurements from balloon soundings indicate a near-surface temperature of −5°C and −20°C near the cloud top. Thus, if liquid is present in the radar echoes, it will be supercooled. It is apparent that from the radar moments it is difficult to infer the cloud phase, although the high radar reflectivity values suggest the presence of ice almost everywhere. The large spectrum width values around 2–2.5 km partially indicate the presence of a particle population with a broad range of velocities and hint at the coexistence of liquid and ice particles; however, this is not a firm criterion for the detection of supercooled liquid since localized turbulence can also affect the spectrum width.

[22] A different view of the same cloud is provided by the lidar (Figure 7). The band of low circular depolarization ratio (CDR) values near the top of the lidar returns is a strong indication of the presence of spherical particles in the sampled volume. The lidar backscatter measurements for the same period also support this conclusion (Figure 7b). A band of high backscatter cross section is present between 1.5 and 2 km, indicating the presence of liquid water that fully attenuates the lidar signal. Four representative spectra from the collocated MMCR are also shown in Figure 7c, corresponding to the indicated times and altitudes of occurrence of Figure 7b. It is apparent that all four spectra are similar and inseparable on the basis of Doppler moments alone. However, the three spectra coinciding with the band of high lidar backscatter have a subtle skewness or bimodality at their principle peaks' left edge, consistent with the presence of liquid, whereas the remaining one (S2) does not.

[23] Using the collocated MMCR Doppler spectra collected during the same period as input to our trained neural network, we predicted the lidar backscatter and CDR and, from these, the region containing supercooled liquid (Figure 8). While our ultimate objective is to retrieve the location of supercooled liquid (Figure 8c), we also display the predicted lidar backscatter and depolarization. The predicted lidar measurements are directly comparable with the actual lidar observations. The cloud ceiling measured independently (not used as

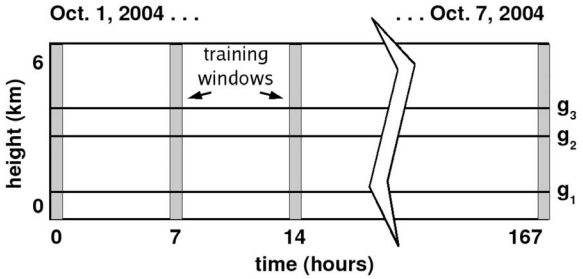

Figure 5. Illustration of the selection scheme for choosing training data. Training data are sparsely sampled from 1 h time windows every 7 h. The population of training samples is distributed evenly over height. Thus, every range gate (g1, g2, g3, …, g*n*) contributes roughly the same number of samples.

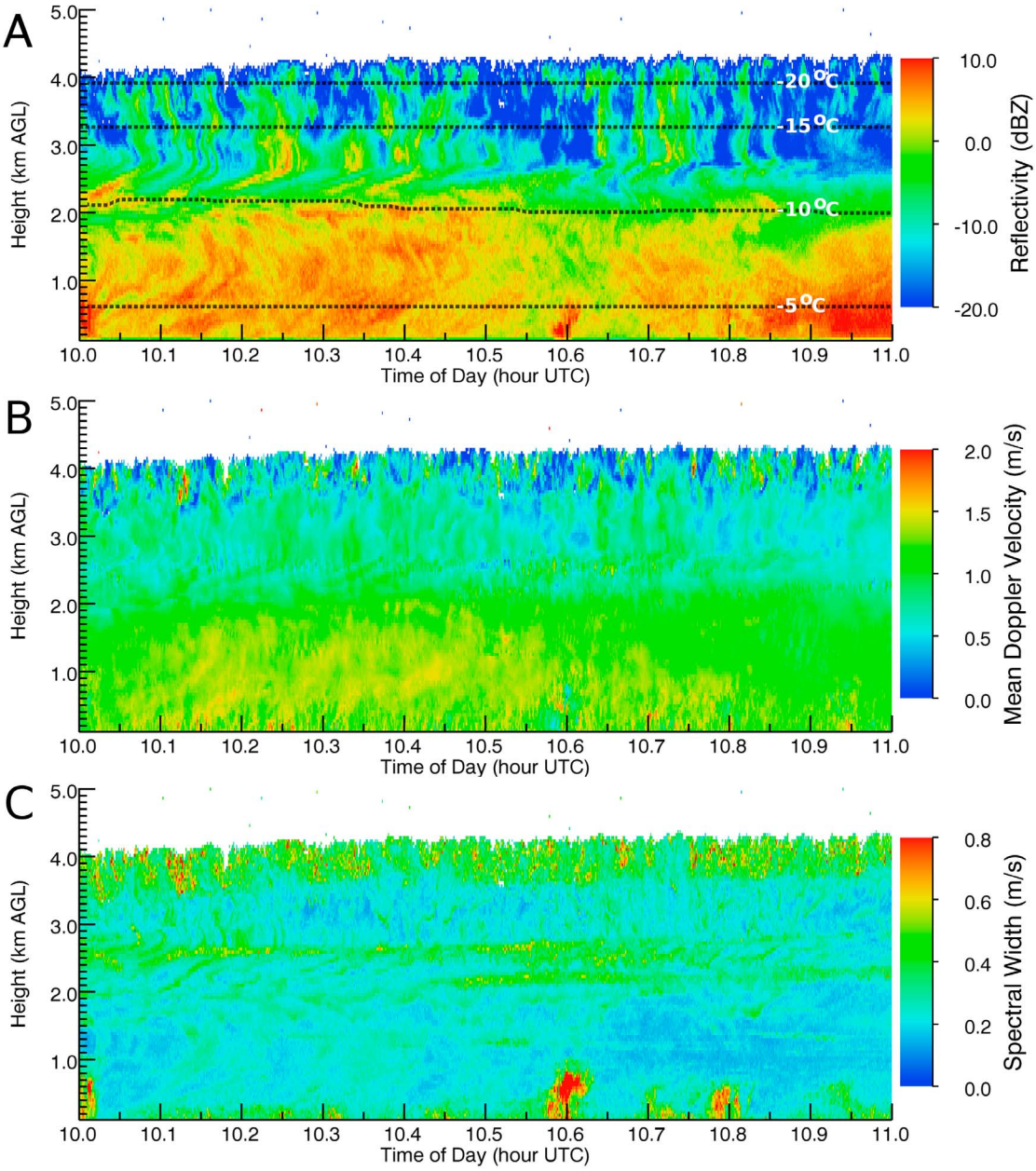

Figure 6. Time-height mapping of MMCR (a) radar reflectivity with radiosonde temperature profile, (b) mean Doppler velocity, and (c) Doppler spectrum width for a 1 h period (1000–1100 UTC) on 7 October 2004.

input to the retrieval) by a collocated ceilometer is overplotted in black. There is excellent morphological consistency between the predicted (Figures 7a and 7b) and observed (Figures 8a and 8b) lidar backscatter and CDR. The lidar measurements in Figure 7 do not extend beyond the layer of high backscatter because of extinction of the lidar beam in optically thick cloud; however, more cloud is present up to about 4 km (Figure 6). The predicted area of supercooled liquid (Figure 8c) suggests the presence of a liquid cloud base around 1.8 km, and inspection shows the reflectivity at this altitude to be in the range of 0 dB. Small liquid droplets alone cannot support such high reflectivity values (e.g., on the order of 10^6 cloud droplets/cm^3 would be required to produce a 0 dBZ radar reflectivity return). Furthermore, the MMCR-based detection of supercooled liquid suggests the presence of pockets of liquid near the cloud top (around 4 km height). Lidar measurements are not available to provide verification for the presence of the liquid layer near the cloud top due to complete lidar signal extinction at the first liquid layer. However, the nearest available balloon sounding to the selected period (taken at 11 UTC) indicates the presence of a thin layer with high relative humidity (above 90%) near the cloud top (Figure 9a). Figure 9b shows the temperature profile from the same sounding.

[24] Another 1 h period that demonstrates the potential to detect cloud liquid and predict lidar observables using

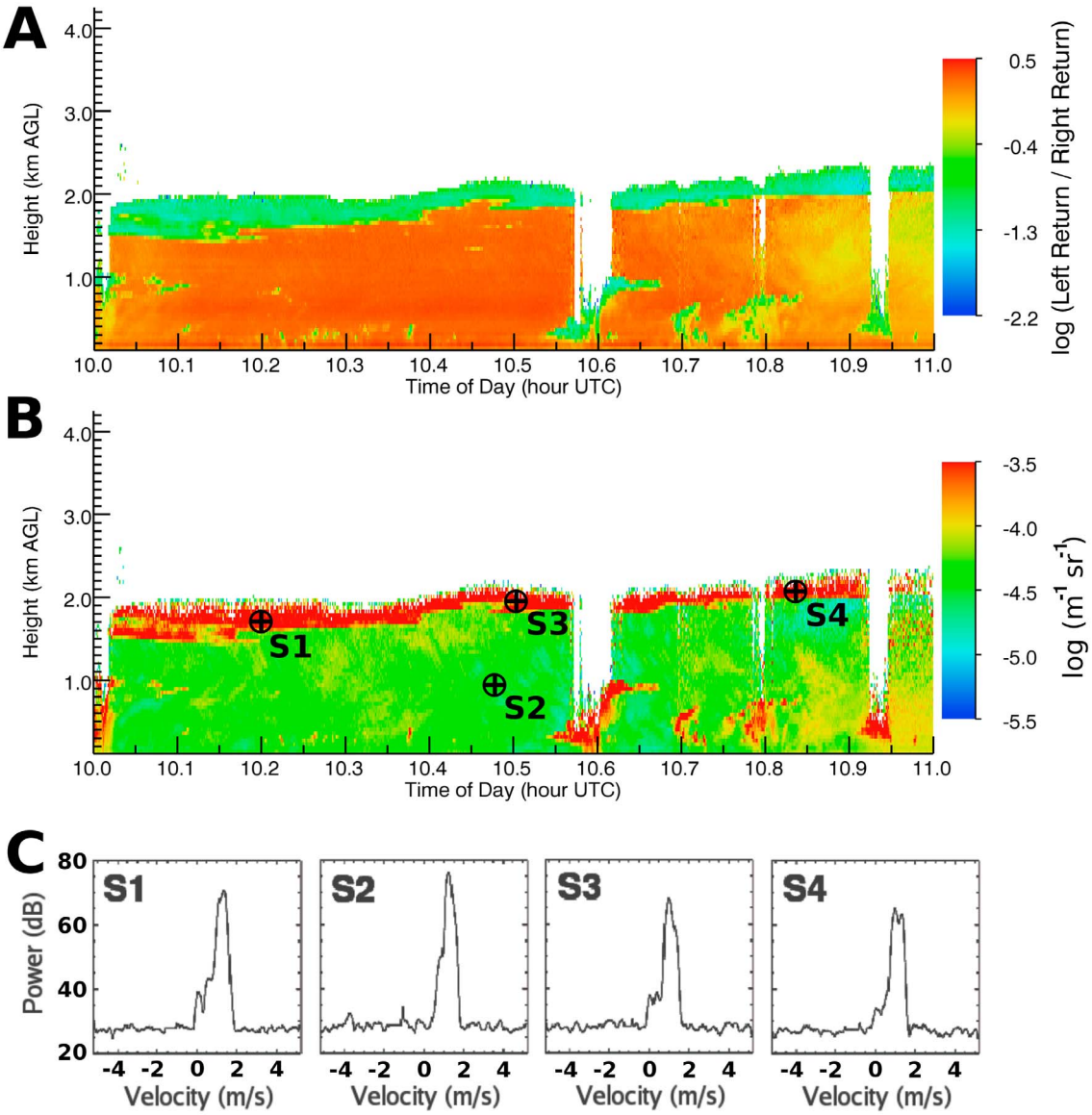

Figure 7. Time-height mapping of (a) the observed lidar circular depolarization ratio (CDR) for 1 h period (1000–1100 UTC) on 7 October, (b) the observed lidar backscatter for the same period, and (c) examples of four MMCR Doppler spectra collected during the same period corresponding to the indicated time-height locations in Figure 7b.

MMCR Doppler spectra is shown in Figures 10 and 11. This case is from a multiliquid layer period with precipitating ice (Figure 10). The observed lidar CDR and backscatter measurements (Figures 10a and 10b) suggest the presence of two liquid layers, but with the upper layer substantially occluded by extinction in the lower layer when compared with the MMCR reflectivity view of the same period (Figure 10c). The predicted lidar backscatter, CDR, and area of supercooled liquid within the range of the radar's operational sensitivity are shown in Figure 11. Once again, there is remarkable consistency between the observed and predicted lidar backscatter, CDR, and location of the supercooled liquid. The independently measured ceilometer cloud base is also shown in Figure 11. Once again, the sharp liquid base predicted from the neural network coincides very well with the ceilometer cloud base and the high backscatter values measured by the lidar. Figure 11 fills out the picture of two liquid layers and even suggests a third layer of mixed-phase conditions (Figure 11c) at 1.2 km, which is also briefly hinted in the actual measurements of Figure 10a at 6.475 UTC.

4.2. Comparisons With Liquid Water Path and Cloud Base Detections

[25] Additional validation of the supercooled liquid detection algorithm is provided through a comparison of our retrieved lowest supercooled liquid layer base and the ceilometer cloud base (Figure 12a) over the entire month of October 2004. Both time series are smoothed by a box-car window filter of 4 h duration. The result shows good agreement over this longer time frame, even though training data

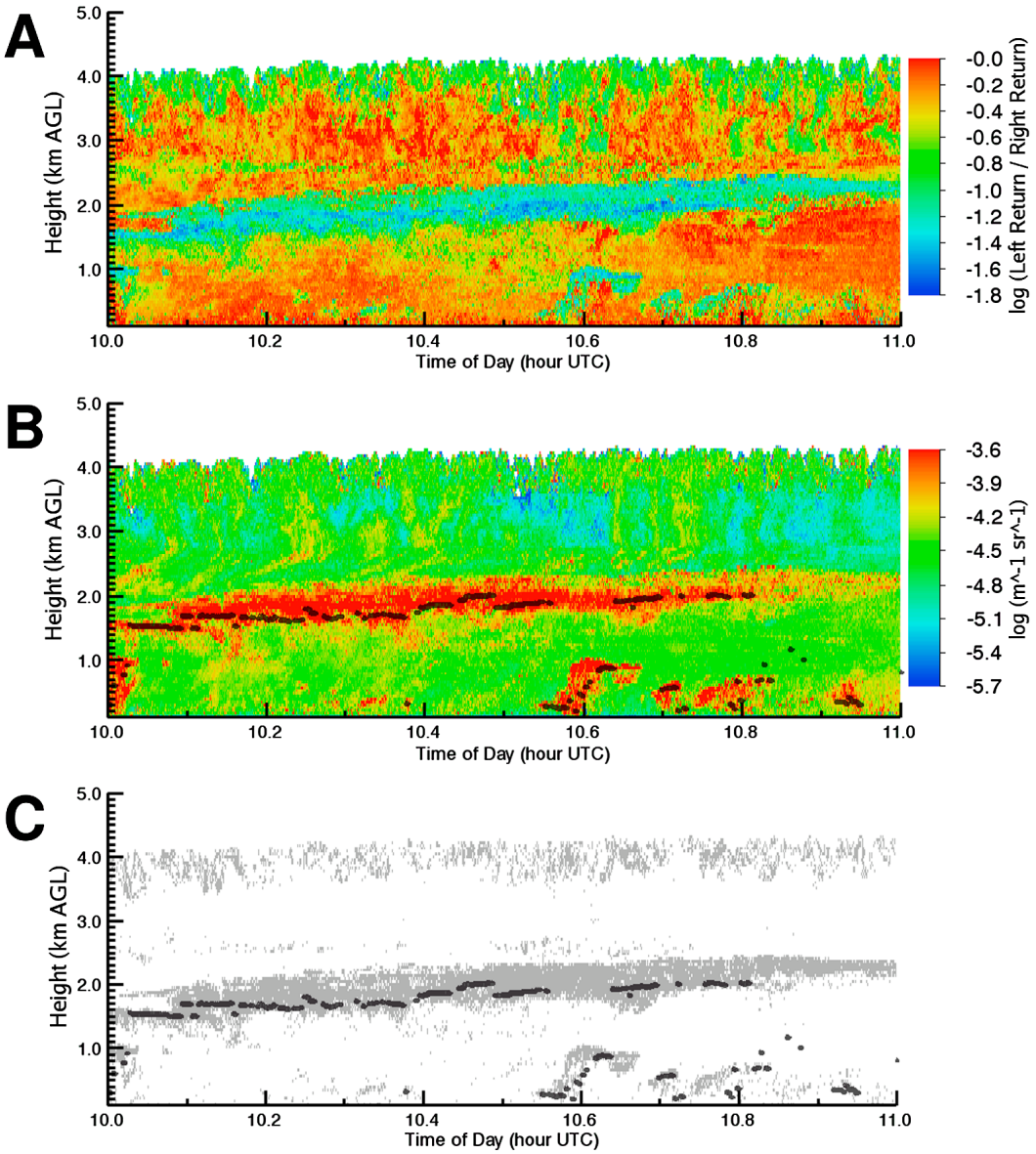

Figure 8. Time-height mapping of (a) the predicted lidar CDR using the corresponding MMCR Doppler spectra for the period 1000–1100 UTC on 7 October 2004, (b) the predicted lidar backscatter for the same period with the ceilometer cloud base (black dots) plotted for reference, and (c) the predicted area of supercooled liquid detections.

was only taken from the first week. That our retrieval technique detects not only the presence of supercooled liquid in the column but also accurately locates the base of the first liquid layer is indicative of its sensitivity to detecting small amounts of liquid, since the smallest amounts of liquid are expected at the cloud base level. For comparison, Figure 12b shows the base of significant radar hydrometeor detections (often the lowest height of the precipitating ice) over the same time period in black and the ceilometer cloud base in gray. These comparisons clearly demonstrate the method's ability to identify liquid water layers embedded in ice.

[26] The ARM suite of instruments operating at NSA during MPACE included a zenith pointing microwave radiometer providing zenith measurements of integrated liquid water path. The gray curve of Figure 12c shows the recorded liquid water path measured by this instrument over the month of October 2004. The overlaid black curve shows the column thickness of our radar-retrieved liquid mask for the same time period. Liquid mask column thickness and Liquid Water Path (LWP) are both smoothed by a box-car window filter of 4 h duration. The correlation between these two time series is 0.68. This correlation is expected to be somewhat less than unity because of the natural variability of liquid as a function of height (i.e., differences in liquid water content). For comparison, we generated a time series of the total column thickness of all significant hydrometeor radar detections (liquid and ice) and found its correlation with the MWR liquid water path over the same time period to be only 0.079. We can infer then that the liquid-containing subset of radar returns has been substantially identified within the full

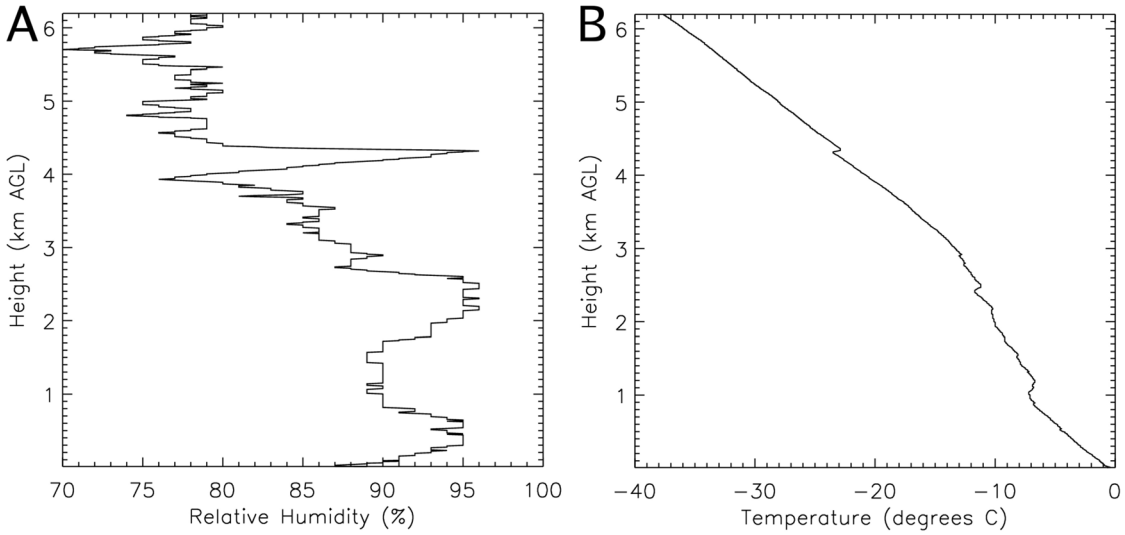

Figure 9. Soundings of (a) relative humidity and (b) temperature at 11 UTC on 7 October 2004.

set of radar returns over the monthlong period. The MWR did not play any role in the training of our algorithm and thus provides an entirely independent source of validation.

[27] Forty percent of our October 2004 radar-retrieved liquid water mask coincides with radar returns having a reflectivity of at least −15 dBZ (Figure 13a). It is interesting to note that when we limit our mask to this higher reflectivity subset, its column thickness correlation with MWR liquid water path actually increases to 0.75. For the column thickness of all hydrometeor radar detections of at least −15 dBZ, the correlation with the MWR liquid water path is 0.2. Once again, we can infer the ability of the technique to locate the liquid containing returns within the higher reflectivity (>−15 dBZ) subset.

[28] Figures 13b and 13c show temperature and relative humidity distributions of sounding measurements for all time-height pixels identified to contain liquid water that are within 1 h of a radiosonde launch during October 2004. The Doppler spectra-based detections of supercooled liquid are found to be within the −30°C–0°C range. This finding agrees with prevailing theories for the existence of supercooled liquid at temperature ranges of −40°C–0°C. Although not a surprise, another interesting finding is that the bulk of our supercooled liquid detections occur in areas with relative humidity higher than 90%.

5. Summary

[29] The life cycles and radiative properties of clouds are highly sensitive to the phase of their hydrometeors (i.e., liquid or ice). Cloud radars are among the premier instruments used in atmospheric research for the detection of the vertical structure of clouds. Conditional analysis of cloud radar Doppler moments can provide limited information for predicting cloud phase; however, the information is inconclusive in a large fraction of mixed-phase conditions. This limitation comes from dependency of the radar backscatter on the sixth power of the hydrometeor diameter resulting in radar return signals being dominated by the presence of large ice crystals and the masking of the supercooled liquid droplet returns.

[30] Synergistic profiling measurements from cloud radars and lidars have been proposed for the identification of cloud phase based on differences in their scattering mechanisms [e.g., *Shupe*, 2007]. High lidar backscatter and near-zero lidar depolarization measurements have been previously found to correlate very well with the presence of liquid layers in clouds. However, such measurements are not widely available and the detection of supercooled liquid is possible only in areas where a lidar signal is available (subject to liquid attenuation).

[31] The proposed technique overcomes this fundamental limitation of cloud radars and suggests new venues for the retrieval of the location of supercooled liquid using vertically pointing cloud radars. The proposed technique hinges on the idea that careful sampling of clouds by vertically profiling cloud radars [*Kollias et al.*, 2007a] can reduce the detrimental effects of dynamics on the Doppler spectrum morphology. The ARM MMCRs are an example of cloud radars where such sampling is implemented and the recorded Doppler spectra contain microphysical signatures. In this study, we used a wavelet operator on the recorded Doppler spectra in order to identify subtle differences in the Doppler spectrum morphologies that can lead to the detection of the presence of more than one water phase in the radar resolution volume.

[32] Using the MMCR Doppler spectra, we detected the area of supercooled liquid in both single and multilayer cloud scenes. The retrieved area of the supercooled liquid nicely agrees with the prediction of supercooled liquid from the lidar measurements. A monthlong time series of predicted liquid column thickness shows high correlation with integrated liquid water path independently measured by a collocated microwave radiometer. The ability of the MMCR to penetrate multilayer clouds enables the prediction of lidar observables in areas where lidar measurements are not available because of signal extinction. This extends the ability of ground-based systems to retrieve cloud phase in areas with

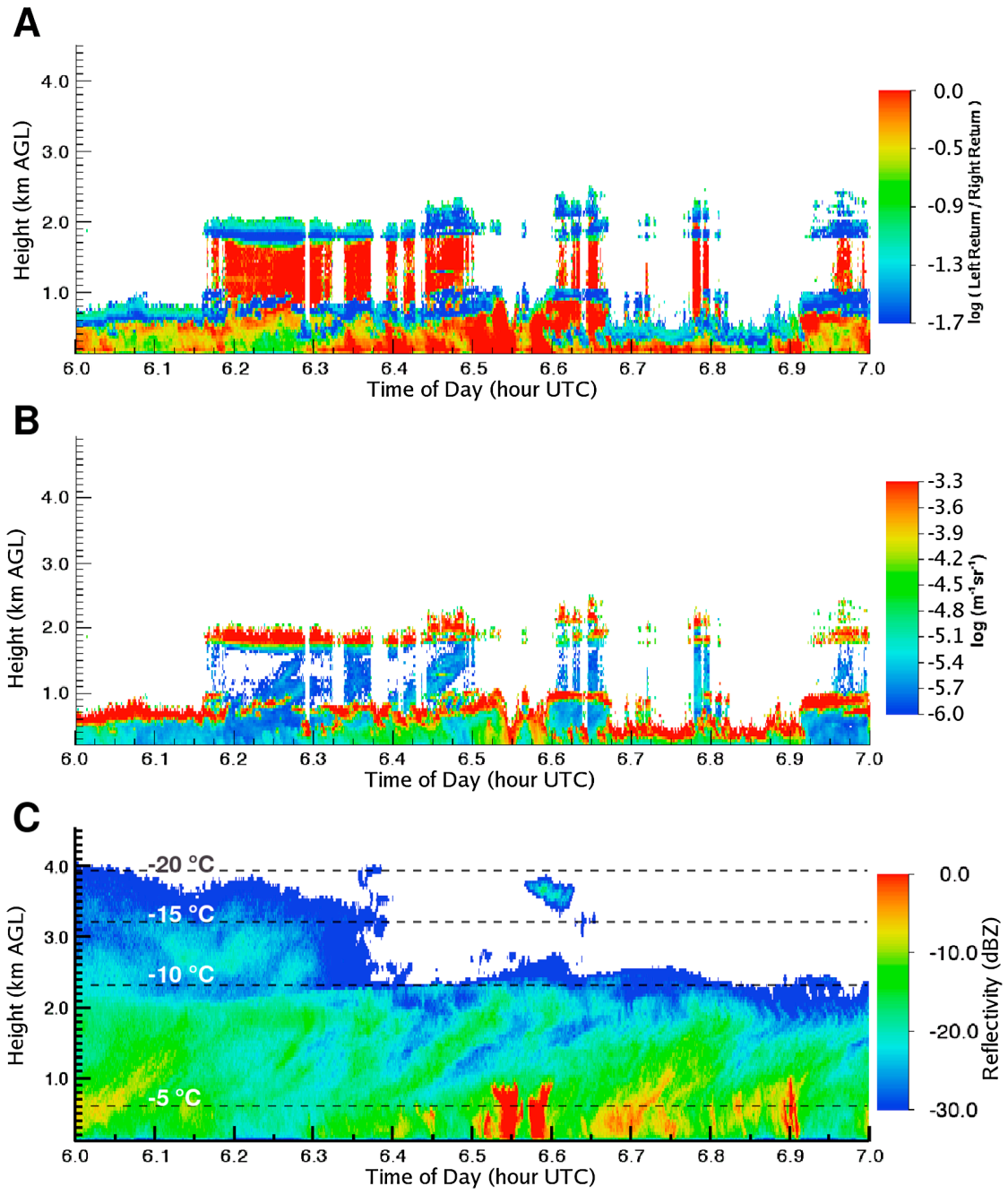

Figure 10. Time-height mapping of (a) the observed lidar circular depolarization ratio (CDR) for 1 h period (0600–0700 UTC) on 7 October, (b) the observed lidar backscatter for the same period, and (c) the observed MMCR radar reflectivity of the same period, with radiosonde temperature profile. This is a multilayer cloud arctic case.

no lidar measurements and without the use of assumptions related to cloud morphology and spatial distribution of cloud phase.

[33] It is not our intent to suggest that the MMCR could replace the lidar observations. The suggested technique provides only information about the presence of supercooled liquid in clouds, while lidar measurements help to extract quantitative microphysical information about the cloud droplets and aerosols that are not possible with a cloud radar. Radar sensitivity is another factor that limits the application of the technique. During the ARM MPACE experiment, some physically thin and low liquid water layers were undetected by the NSA MMCR. Thus, our radar-based technique is applicable only to areas where the liquid radar return is above the detection threshold of the cloud radar. Plans include the application of the technique to all the ARM sites using appropriate training data sets (e.g., micropulse and Raman lidar measurements).

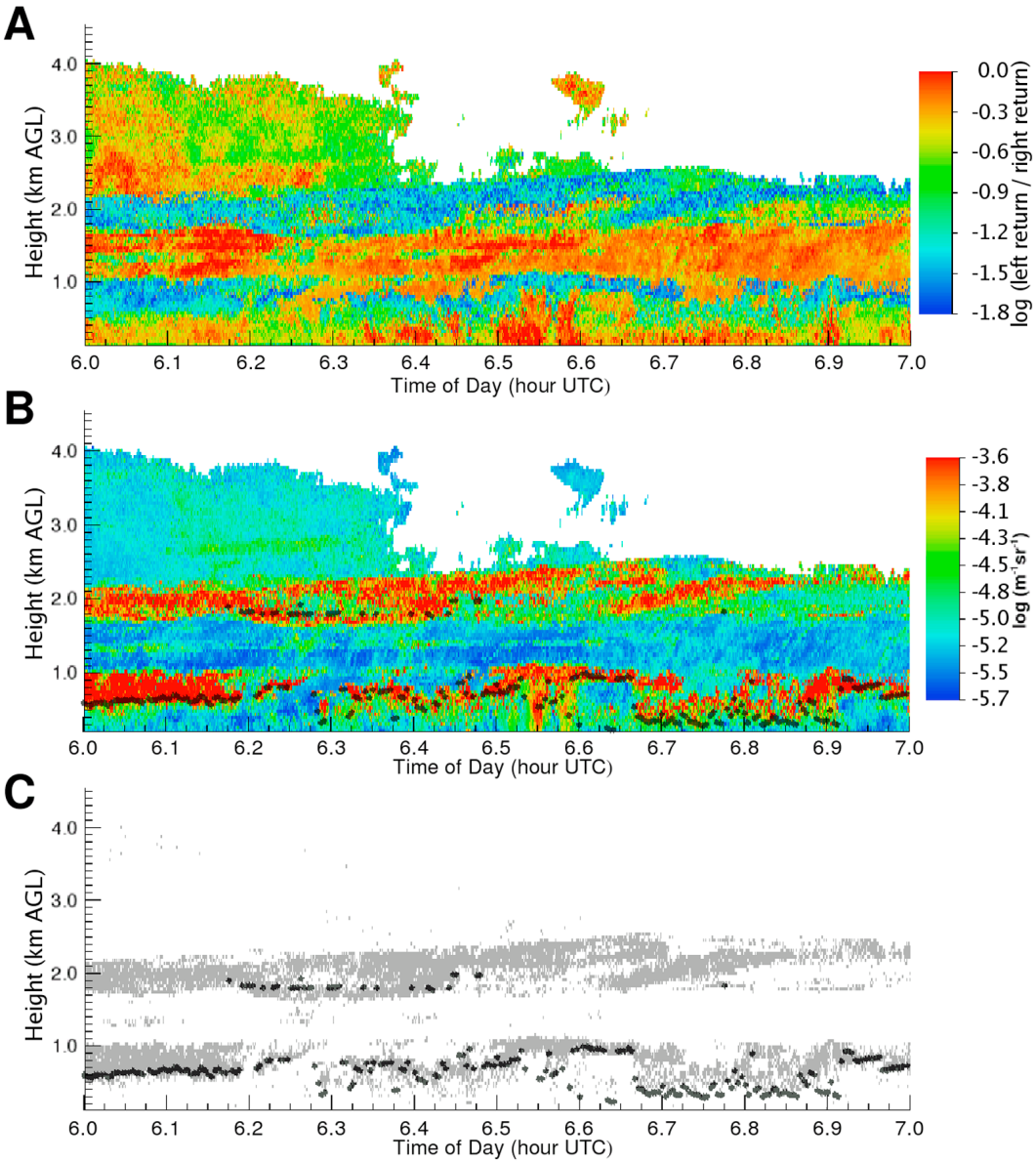

Figure 11. Time-height mapping of (a) the predicted lidar CDR using the corresponding MMCR Doppler spectra for the period 0600–0700 UTC on 7 October 2004, (b) the predicted lidar backscatter for the same period with the ceilometer cloud base (black dots) plotted for reference, and (c) the predicted area of supercooled liquid detections.

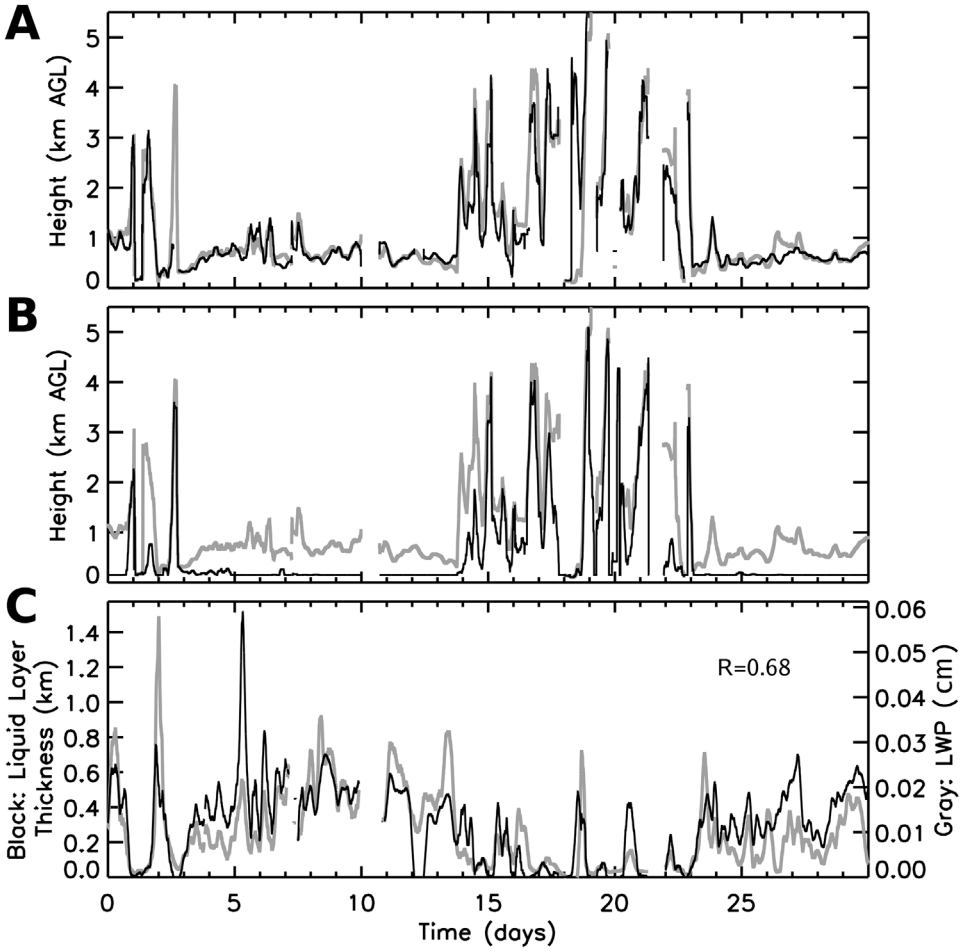

Figure 12. Time series of (a) ceilometer measured cloud base (gray) and the base of radar retrieved liquid (black), (b) ceilometer measured cloud base (gray) and the base of significant radar detections (black), and (c) MWR measured liquid water path (gray) and column thickness of the radar retrieved liquid mask (black), in km, for October 2004. MWR LWP has a 0.68 correlation with retrieved liquid thickness.

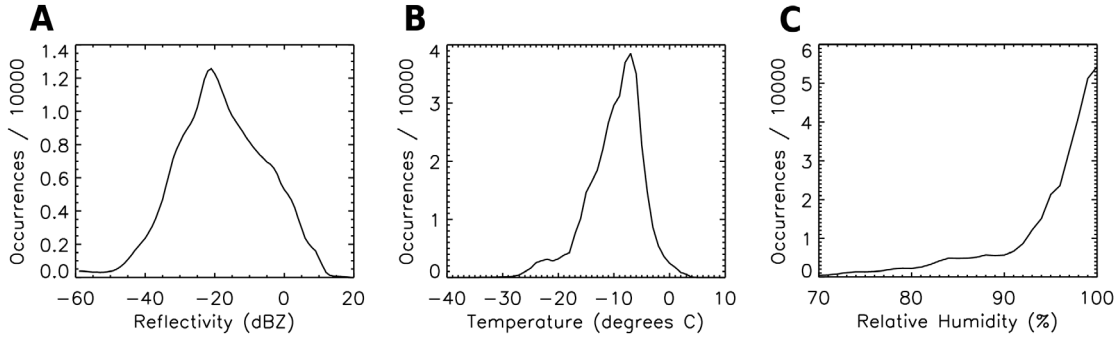

Figure 13. (a) Reflectivity, (b) temperature, and (c) relative humidity distributions of the October 2004 radar retrieved liquid mask pixels occuring within 1 h of a radiosonde launch.

[34] The application of wavelets or other operators to the recorded Doppler spectra can lead to new ways of analyzing radar Doppler spectra. Already, the ARM program is producing higher moments of the Doppler spectra (such as skewness and kurtosis) and identifying the presence of spectral multimodalities. In many cases, these parameters all exhibit good coherence in time and space and open new venues for process studies in clouds and precipitation using radars.

[35] Additional validation of the proposed retrieval technique and detailed assessment of related uncertainties should be the focus of future work. These can be achieved in the context of future field campaigns with comprehensive instrumentation and at a variety of locations.

[36] **Acknowledgments.** This research was supported by the Office of Science (BER), U. S. Department of Energy, grant DE-FG02-05ER63965. Data were obtained from the ARM archive and University of Wisconsin.

References

Ackerman, T. P., and G. Stokes (2003), The Atmospheric Radiation Measurement program, *Phys. Today*, *56*, 38–45.

Addison, P. S. (2002), *The Illustrated Wavelet Transform Handbook*, Institute of Physics Publishing Ltd., London.

Cober, S. G., G. A. Issac, and J. W. Strapp (2001), Characterization of aircraft icing environments that include supercooled large drops, *J. Appl. Meteorol.*, *40*, 1984–2002.

Curry, J. A. (1986), Interactions among turbulence, radiation and microphysics in Arctic stratus clouds, *J. Atmos. Sci.*, *43*, 90–106.

Eloranta, E. W. (2005), High Spectral Resolution Lidar, in *Lidar: Range-Resolved Optical Remote Sensing of the Atmosphere*, edited by K. Weitkamp, Springer-Verlang, New York.

Frisch, A. S., C. W. Fairall, and J. B. Snider (1995), Measurement of stratus cloud and drizzle parameters in ASTEX with a Ka-band Doppler radar and a microwave radiometer, *J. Atmos. Sci.*, *52*, 2788–2799.

Funahashi, K. (1989), On the approximate realization of continuous mappings by neural networks, *Neural Networks*, *2*, 183–192.

Gosset, M., and H. Sauvageot (1992), A dual-wavelength radar method for ice-water characterization in mixed-phase clouds, *J. Atmos. Oceanic Technol.*, *9*, 538–547.

Hobbs, P. V., and A. L. Rangno (1985), Ice particle concentrations in clouds, *J. Atmos. Sci.*, *42*, 2523–2549.

Hobbs, P. V., and A. R. Rangno (1998), Microstructures of low and middle-level clouds over the Beaufort Sea, *Q. J. R. Meteorol. Soc.*, *124*, 2035–2071.

Hogan, R. J., P. N. Francis, H. Flentje, A. J. Illingworth, M. Quante, and J. Pelon (2003), Characteristics of mixed-phase clouds: Part I. Lidar, radar and aircraft observations from CLARE'98, *Q. J. R. Meteorol. Soc.*, *129*(592), 2089–2116.

Hogan, R. J., M. D. Behera, E. J. O'Connor, and A. J. Illingworth (2004), Estimate of the global distribution of stratiform supercooled liquid water clouds using the LITE lidar, *Geophys. Res. Lett.*, *31*, L05106, doi:10.1029/2003GL018977.

Intrieri, J. M., M. D. Shupe, T. Uttal, and B. J. McCarty (2002), An annual cycle of Arctic cloud characteristics observed by radar and lidar at SHEBA, *J. Geophys. Res.*, *107*(C10), 8030, doi:10.1029/2000JC000423.

Kollias, P., B. A. Albrecht, R. Lhermitte, and A. Savtchenko (2001), Radar observations of updrafts, downdrafts, and turbulence in fair weather cumuli, *J. Atmos. Sci.*, *58*, 1750–1766.

Kollias, P., B. A. Albrecht, and F. Marks (2002), Why Mie? *Bull. Am. Meteorol. Soc.*, *83*(10), 1471–1483.

Kollias, P., E. E. Clothiaux, M. A. Miller, E. P. Luke, K. L. Johnson, K. P. Moran, K. B. Widener, and B. A. Albrecht (2007a), The Atmospheric Radiation Measurement Program cloud profiling radars: Second-generation sampling strategies, processing, and cloud data products, *J. Atmos. Oceanic Technol.*, *24*, 1199–1214.

Kollias, P., E. E. Clothiaux, M. A. Miller, B. A. Albrecht, G. L. Stephens, and T. P. Ackerman (2007b), Millimeter-wavelength radars – New frontier in atmospheric cloud and precipitation research, *Bull. Am. Meteorol. Soc.*, *88*, 1608–1624.

Korolev, A. V., G. A. Isaac, S. G. Cober, J. W. Strapp, and J. Hallett (2003), Microphysical characterization of mixed-phase clouds, *Q. J. R. Meteorol. Soc.*, *129*(587), 39–65.

Lawson, P., B. A. Baker, C. G. Schmitt, and T. L. Jensen (2001), An overview of microphysical properties of Arctic clouds observed in May and July 1998 during FIRE ACE, *J. Geophys. Res.*, *106*, 14,989–15,014, doi:10.1029/2000JD900789.

Maykut, G. A., and N. Untersteiner (1971), Some results from a time-dependent thermodynamic model of sea ice, *J. Geophys. Res.*, *76*, 1550–1575, doi:10.1029/JC076i006p01550.

Moran, K. P., B. E. Martner, M. J. Post, R. A. Kropfli, D. C. Welsh, and K. B. Widener (1998), An unattended cloud-profiling radar for use in climate research, *Bull. Am. Meteorol. Soc.*, *79*, 443–455.

Pinto, J. O. (1998), Autumnal mixed-phase cloudy boundary layers in the Arctic, *J. Atmos. Sci.*, *55*, 2016–2038.

Rioul, O., and M. Vetterli (1991), Wavelets and signal processing, *IEEE Signal Process. Mag.*, *8*, 14–38.

Rumelhart, D. E., G. E. Hinton, and R. J. Williams (1986), Learning representations by back-propagating errors, *Nature*, *323*, 533–536, doi:10.1038/323533a0.

Sassen, K., C. J. Grund, J. D. Spinhirne, M. M. Hardesty, and J. M. Alvares (1990), The 27–28 October 1986 FIRE IFO Case Study: A five lidar overview of cloud structure and evolution, *Mon. Weather Rev.*, *118*, 2288–2311.

Sekelsky, S. M., and R. E. McIntosh (1996), Cloud observations with polarimetrc 33 GHz and 95 GHz radar, *Meteorol. Atmos. Phys.*, *59*, 123–140.

Shupe, M. D. (2007), A ground-based multiple remote-sensor cloud phase classifier, *Geophys. Res. Lett.*, *34*, L22809, doi:10.1029/2007GL031008.

Shupe, M. D., and J. M. Intrieri (2004), Cloud radiative forcing of the Arctic surface: The influence of cloud properties, surface albedo, and solar zenith angle, *J. Clim.*, *17*, 616–628.

Shupe, M. D., P. Kollias, S. Y. Matrosov, and T. L. Schneider (2004), Deriving Mixed-Phase Cloud Properties from Doppler Radar Spectra, *J. Atmos. Oceanic Technol.*, *21*, 660–670.

Shupe, M. D., S. Y. Matrosov, and T. Uttal (2006), Arctic mixed-phase cloud properties derived from surface-based sensors at SHEBA, *J. Atmos. Sci.*, *63*, 697–711.

Shupe, M. D., J. S. Daniel, G. de Boer, E. W. Eloranta, P. Kollias, C. N. Long, E. P. Luke, D. D. Turner, and J. Verlinde (2008), A focus on mixed-phase clouds, *Bull. Am. Meteorol. Soc.*, *89*, 1549–1562.

Stamnes, K., R. G. Ellingson, J. A. Curry, J. E. Walsh, and B. D. Zak (1999), Review of science issues and deployment strategies for the North Slope of Alaska/Adjacent Arctic Ocean (NSA/AAO) ARM site, *J. Clim.*, *12*, 46–63.

Turner, D. D. (2005), Arctic mixed-phase cloud properties from AERI lidar observations: Algorithm and results from SHEBA, *J. Appl. Meteorol.*, *44*, 427–444.

Verlinde, H., and Coauthors (2007), The Mixed-Phase Arctic Cloud Experiment (MPACE), *Bull. Am. Meteorol. Soc.*, *88*, 205–221.

Wang, X., and J. Key (2003), Recent trends in Arctic surface, cloud, and radiation properties from space, *Science*, *299*(5613), 1725–1728.

Wang, Z., K. Sassen, D. N. Whiteman, and B. B. Demoz (2004), Studying altocumulus with ice virga using ground-based active and passive remote sensors, *J. Appl. Meteorol.*, *43*, 449–460.

Wendisch, M., A. Keil, and A. V. Korolev (1996), FSSP characterization with monodisperse water droplets, *J. Atmos. Oceanic Technol.*, *13*, 1152–1165.

Zhang, T., K. Stamnes, and S. A. Boxling (1996), Impact of clouds on surface radiative fluxes and snowmelt in the Arctic and sub-Arctic, *J. Climate*, *9*, 2110–2123.

P. Kollias, Department of Atmospheric and Oceanic Sciences, McGill University, 805 Sherbrooke St. W., Montreal, QC H3A 2K6, Canada.

E. P. Luke, Atmospheric Sciences Division, Brookhaven National Laboratory, Building 490D, Bell Avenue, Upton, NY 11973, USA. (eluke@bnl.gov)

M. D. Shupe, Cooporative Institute for Research in Environmental Sciences, University of Colorado and NOAA Earth System Research Laboratory, 325 Broadway, R/PSD3, Boulder, CO, USA.